

Sintering of Alumina Nanoparticles: Comparison of Interatomic Potentials, Molecular Dynamics Simulations, and Data Analysis

S. Roy^{1,2†}, A. Prakash^{2 †}, and S. Sandfeld^{1,2,3,4}

¹Institute for Advanced Simulation: Materials Data Science and Informatics (IAS-9), Forschungszentrum Juelich GmbH, 52425 Juelich, Germany

²Chair of Micromechanical Materials Modelling (MiMM), Institute of Mechanics and Fluid Dynamics, TU Bergakademie Freiberg, 09599 Freiberg, Germany

³JARA, Forschungszentrum Juelich GmbH, 52425 Juelich, Germany

⁴Chair of Materials Data Science and Materials Informatics Faculty 5, RWTH Aachen University, 52056 Aachen, Germany

E-mail: s.sandfeld@fz-juelich.de

Abstract. Sintering of alumina nanoparticles is of interest both from the view of fundamental research as well as for industrial applications. Atomistic simulations are tailor-made for understanding and predicting the time- and temperature-dependent sintering behaviour. However, the quality and predictability of such analysis is strongly dependent on the performance of the underlying interatomic potentials. In this work, we investigate and benchmark four empirical interatomic potentials and discuss the resulting properties and drawbacks based on experimental and density functional theory data from the literature. The potentials, which have different origins and formulations, are then used in molecular dynamics simulations to perform a systematic study of the sintering process. To analyse the results, we develop a number of tailored data analysis approaches that are able to characterise and quantify the sintering process. Subsequently, the disparities in the sintering behaviour predicted by the potentials are critically discussed. Finally, we conclude by providing explanations for the differences in performance of the potentials, together with recommendations for molecular dynamics sintering simulations of alumina.

Keywords: alumina, interatomic potential, ionic potential, molecular dynamics simulations, sintering, data analysis

Submitted to: *Modelling Simul. Mater. Sci. Eng.*

† These authors contributed equally.

† These authors contributed equally.

1. Introduction

Aluminium oxide (Al_2O_3) or *alumina* has evoked significant research interest due to its use in technological and industrial applications, ranging from the field of aerospace [1], water treatment, filtration and cooling systems [2–4], medical and health care [5–7], to materials engineering [8–10]. Alumina coating on aluminium is known to improve wear resistance [11] and act as electrical and thermal insulation [12]. The material exhibits unique properties, such as e.g., high thermal conductivity, high hardness, and a good resistance to corrosion and abrasion [13].

An important technique for processing alumina is sintering, which involves consolidation and densification of powder compacts, and is driven by a reduction in total interface energy [14]. As one of the technologies that has been known and used for a long time, the process has proven to be important and beneficial for the production of a variety of ceramic structures, from powder-metallurgy parts to bulk components. Recently, sintering has evoked much interest in modern industrial production technologies such as 3D printing and additive manufacturing.

Accurate modelling of the sintering process is on the wish list of many sintering industries, mainly due to the engineering expediency it provides. However, the complex interplay of a multitude of parameters together with a lack of fundamental materials understanding at the nanoscale have proven to be a major hindrance to this end [15].

Indeed, many of the benefits and applications of alumina have their origins at the nanoscale making the material system and the sintering process ideally suited for investigation with atomistic modelling and simulations. Such simulations, which follow the trajectory of individual atoms, have now established themselves as an indispensable tool in advancing our understanding of materials behavior [16–18]. Sintering and concomitant processes have been investigated through molecular dynamics (MD) simulations for a large variety of materials (including alumina) and for a number of different techniques such as selective laser sintering or pressure-assisted/pressure-less sintering [19–21].

Atomistic modelling of materials behavior is, however, not straightforward and hinges primarily on three aspects [18]: i) accuracy of the initial structure used, ii) reflection of real-world boundary conditions, and most importantly, iii) the reliability, robustness and predictive capability of the interatomic potential used. Such interatomic potentials are particularly critical for oxide materials such as alumina due to the ionic (and partly covalent) nature of the oxygen-metal bonds, which require the inclusion of long-range effects. Although many interatomic potentials for alumina exist, each potential is developed with a different rationale in terms of applicability and transferability. The choice of the interatomic potential hence becomes crucial for the atomistic study, and is usually made by evaluating the predictive capability of the potential on certain basic material properties – e.g., lattice constants, cohesive and surface energies and elastic constants – and subsequently applied to

the more complex problem at hand.

Aluminium oxide often exists in crystalline form – the *corundum structure* – and is a member of the hexagonal close packed (hcp) family. A single molecule consists of two aluminium and three oxygen atoms, the interactions among which are usually modelled by incorporating two-body and/or three-body interaction terms. The Coulomb-Buckingham [22] or Born-Mayer-Huggins type potentials [23] are based purely on two-body interactions, whilst the potential by Vashishta *et al.* [24] incorporates both two-body and three-body interactions, with the latter associated with triplets containing Al-O bonds. A common feature of such potentials is the usage of fixed charges – both nominal and effective – for Al and O ions. To account for local heterogeneous electrostatic environment, particularly in the presence of interfaces, free surfaces and segregated ions, improvements have been proposed by incorporating variable point charges. Reactive potentials, such as reactive empirical bond order (REBO), reactive force field (ReaxFF) and charge optimised bond order (COMB) potentials, integrate many-body effects and two-body interactions through a bond order term [25]. Other approaches such as the charge-transfer ionic [26] and the second-moment tight-binding [27] models are simpler in their approach and allow for charge equilibration during the process under study.

In this work, we investigate the sintering of spherical nanoparticles using molecular dynamics simulations. Specifically, we compare four different interatomic potentials – the Vashishta potential [24], the Coulomb-Buckingham potential of the Matsui type [28], the Born-Mayer-Huggins potential parametrised by Bouhadja *et al.* [23] and the charge transfer ionic potential [26]. We first present the mathematical formulations of the potentials and evaluate the predictive capability of these potentials towards basic material properties. Subsequently, the sintering process is simulated for three different temperatures by considering spherical nanoparticles of three different sizes. Sintering is modelled as isothermal, high temperature process. In other words, we neglect pressure effects that play an important role in low temperature sintering [29–31]. We develop a data analysis strategy that is based on a number of atomic and geometric properties to quantify and characterize the process. As a result, we find that despite exhibiting similar material properties, the investigated potentials result in very different sintering outcomes. We then discuss the characteristics used in terms of their ability to clearly quantify the progress of sintering by setting numerical thresholds.

In the following section, we start by introducing the used potentials and rewrite them in a consistent mathematical formulation. Subsequently, details of modelling, simulation, and data analysis for characterising sintering are provided. We then compare various alumina properties (such as elastic properties, surface energies, lattice parameters, etc.) that result from our atomistic simulations with data from experiments and density functional theory calculations. The actual sintering simulations are analysed in detail for all four potentials, which is concluded by a discussion of their respective suitability and appropriateness for MD

simulations of nanoparticle sintering of alumina.

2. Interatomic potentials of alumina

In the following, four interatomic potentials are considered for the sintering study: the Vashishta potential (in the following abbreviated as VASH), the Coulomb-Buckingham potential (CB), Born-Mayer-Huggins potential (BMH), and the Charge Transfer Ionic + EAM potential (CTIE). Whilst the last three are based on two-body interactions, the first one, i.e. VASH is based on both two-body and three-body interactions. Three potentials (VASH, BMH, and CB), have the same fixed charges for the anions and cations, and one (CTIE), allows for variable charges. In the following, all the potentials used in our study are briefly introduced.

2.1. Three-body + two-body interaction potential: the Vashishta potential

Developed by Vashishta *et al.* [24], VASH is an interatomic potential based on three-body interaction among Al and O atoms as O-Al-Al and Al-O-O as well as two-body interaction as Al-Al, O-O and Al-O. It reads

$$U = \sum_{i<j} U_{ij}^{(2)}(r_{ij}) + \sum_{i,j<k} U_{jik}^{(3)}(r_{ij}, r_{ik}), \quad (1)$$

where the two-body part ($U_{ij}^{(2)}(r_{ij})$) of the effective potential is written as

$$U_{ij}^{(2)}(r) = \frac{H_{ij}}{r^{\eta_{ij}}} + \frac{Z_i Z_j}{r_{ij}} \exp(-r_{ij}/\lambda) - \frac{D_{ij}}{2r_{ij}^4} \exp(-r_{ij}/\zeta) - \frac{W_{ij}}{r_{ij}^6}. \quad (2)$$

Here, H_{ij} is the strength of the steric repulsion, Z_i the effective charge (in units of the electronic charge $|e|$), D_{ij} is the strength of charge-dipole attraction, W_{ij} is the van der Waals interaction strength, η_{ij} the exponents of the steric repulsion term, $r_{ij} = |\mathbf{r}_i - \mathbf{r}_j|$ the distance between the i^{th} and j^{th} atoms, and λ and ζ are the screening lengths for Coulomb and charge-dipole terms, respectively. The two-body interaction potential includes steric size effects of the ions, charge-transfer effects leading to Coulomb interactions, charge-dipole interactions due to the electronic polarisability of ions and induced dipole-dipole van der Waals interactions. It has a cut off at r_c ($r_c = 6 \text{ \AA}$ for alumina) beyond which the tow-body term is zero. The three-body term is as follows:

$$U_{jik}^{(3)}(r_{ij}, r_{ik}) = R^{(3)}(r_{ij}, r_{ik}) P^{(3)}(\theta_{jik}), \quad (3)$$

where

$$R^{(3)}(r_{ij}) = B_{jik} \exp\left(\frac{\gamma}{r_{ij} - r_0} + \frac{\gamma}{r_{ik} - r_0}\right) \Theta(r_0 - r_{ij}) \Theta(r_0 - r_{ik}), \quad (4)$$

$$P^{(3)}(\theta_{jik}) = \frac{(\cos \theta_{jik} - \cos \bar{\theta}_{jik})^2}{1 + C_{jik} (\cos \theta_{jik} - \cos \bar{\theta}_{jik})^2}. \quad (5)$$

In Eq. 3, 4 and 5, B_{jik} is the strength of the interaction, θ_{jik} the angle formed by \mathbf{r}_{ij} and \mathbf{r}_{ik} , C_{jik} and $\bar{\theta}_{jik}$ are constants, and $\Theta(r_0 - r_{ij})$ is a step function. The three-body term becomes zero when $\theta_{jik} = \bar{\theta}_{jik}$.

2.2. Two-body interaction potentials

2.2.1. The Coulomb-Buckingham potential The (CB) potential consists of of long range (Coulomb) and short range (Buckingham) potential terms as shown in Eq 6.

$$U_{ij}(r_{ij}) = U_{\text{long}}^{\text{Coulomb}} + U_{\text{short}}^{\text{Buckingham}} = \frac{1}{4\pi\epsilon_0} \frac{Z_i Z_j}{r_{ij}} + A_{ij} \exp\left(\frac{-r_{ij}}{\rho_{ij}}\right) - \frac{C_{ij}}{r_{ij}^6}, \quad (6)$$

where Z_i and Z_j are the effective charges, A_{ij} and ρ_{ij} are the parameters of repulsion, r_{ij} is the distance between the i^{th} and j^{th} atoms, C_{ij} is the Van der Waals constant. The exponential term in the CB potential provides a better description of strong repulsion due to the overlap of the closed shell electron clouds, which is vital in a simulation of bombardment by energetic atoms or ions, etc. When atoms lie in a crystalline environment, the distance between two atoms is small, and the short-range potential plays an important role. However, when atoms are far from the substrate (free atoms), the larger distances between atoms leads to a rapid reduction of the short-range contribution and the long-range potential has the dominant effect on the free atoms. This potential can be categorised as [22]

- (i) partial-charge ($Al^{+1.4175}, O^{-0.945}$) Buckingham-type Matsui [28]
- (ii) full-charge (Al^{+3}, O^{-2}) Buckingham-type Bacorisen potential [32]
- (iii) full-charge (Al^{+3}, O^{-2}) Buckingham-type Sun potential [33]
- (iv) BKS (Beest-Krammer-Santen) potential; which is another CB type potential [34].

In the current study we use as CB potential the Matsui type.

2.2.2. The Born-Mayer-Huggins or Tosi/Fumi potential The BMH potential consists of long range (Coulomb) and a short range interactions terms,

$$U_{ij} = \frac{1}{4\pi\epsilon_0} \frac{Z_i Z_j}{r_{ij}} + A \exp\left(\frac{\sigma - r_{ij}}{\rho}\right) - \frac{C}{r_{ij}^6} + \frac{D}{r_{ij}^8}, \quad (7)$$

where σ is an interaction-dependent length parameter, ρ is an ionic-pair dependent length parameter. The first term represents the long-range Coulomb interaction with charges Z_i and Z_j between i^{th} and j^{th} ions, separated by r_{ij} . The last three terms on the right hand side represent the Born repulsive, van der Waals and dipole dispersion interactions, respectively. In the current study, we use this potential parameterised by [23].

‡ Implementation of CB and BMH potentials in LAMMPS requires cut-off distances for non-coulombic and coulombic interactions, and 10 and 15 Å are used as cut-off values for those, respectively.

2.2.3. *The Charge Transfer Ionic + EAM potential* The CTIE potential consists of contributions of the non-ionic interaction and those of the ionic interaction and charge transfer [26, 35],

$$U_{ij} = U_{ij}^{\text{CTI}} + U_{ij}^{\text{EAM}}, \quad (8)$$

where U^{CTI} is the CTIE potential for ionic interaction and charge transfer, and U^{EAM} is the non-ionic interaction. The first part becomes zero for non-electrostatic material. The electrostatic part can be expressed as:

$$U_{ij}^{\text{CTI}} = U_0 + \sum_i q_i \chi_i + \frac{1}{2} \sum_{i,j} q_i q_j V_{ij}, \quad (9)$$

with,

$$\chi_i = \chi_0 + \sum_j Z_i \left(\frac{j}{f_i} - \frac{f_i}{f_j} \right), \quad (10)$$

$$V_{ij} = J_i^0 \delta_{ij} + \sum_{r_i} \frac{f_i}{f_j}, \quad (11)$$

$$f_i = f_i(|r - r_i|) = \frac{\zeta^3}{\pi} \exp(-2\zeta r - r_i). \quad (12)$$

The pair potential is written as

$$U_{ij}^{\text{EAM}} = \frac{1}{2} \sum_{i=1}^N \sum_{j=i}^{i_N} \phi_{ij}(r_{ij}) + \sum_{i=1}^N F_i(\rho_i), \quad (13)$$

where $\phi_{ij}(r_{ij})$ is the pair energy between the i^{th} and j^{th} atom separated by r_{ij} , $F_i(\rho_i)$ is the embedding energy to embed an atom i in a local site with electron charge density ρ_i . More details are given in [26, 35].

2.2.4. *A first juxtaposition of the four potentials* From the above equations we observe the following: The formulations of CB and BMH are mathematically similar and become identical if D is zero in Eq. 7. They both are two-body interaction potentials. However, in the two-body interaction of the VASH potential, there are two additional terms for steric repulsion and charge-dipole interaction. The additional term for three-body interaction incorporated in VASH contains spatial and angular dependent factors, which is useful for amorphous alumina [24]. The three-body term applies to triplets Al-O-Al and O-Al-O with fixed angles. The charges are fixed and the same for anions and cations in all these potential. By contrast, CTIE is a potential of variable charges, where charges of two anions or cations are not identical. Numerical values of the parameters used in the four potentials are tabulated in the *Appendix*.

3. Methods

All simulations are performed using the Large-scale Atomic/Molecular Massively Parallel Simulator (LAMMPS) atomistic simulation software [36]. Molecular statics (MS) is employed to calculate and verify basic potential properties of individual potentials, and molecular dynamics is employed to determine the melting temperature and to simulate sintering. A stable time step of 1 fs is used in all MD simulations.

3.1. Material properties at 0 K

Five different properties of the interatomic potentials, viz., lattice constants, cohesive energy, vacancy formation energies, elastic constants and surface energies, are calculated using standard procedures via MS simulations. Further details are provided in the *supplementary material*.

3.2. Melting temperature

The melting temperature of alumina for the different potentials is determined using standard molecular dynamics simulations via the following procedure. A 3D triclinic sample of size $33 \times 29 \times 39 \text{ \AA}$ and an xy tilt factor of 16.7 \AA consisting of 1764 Al and 2746 O atoms and periodic boundary conditions in all directions is thermalised at several targeted temperatures using the isobaric isothermal (NPT) ensemble. The average atomic volume, determined via a Voronoi tessellation as implemented in the open visualisation tool OVITO, is plotted for the different target temperatures. The melting point for the system and potential is then approximated as the temperature at which a jump in the average atomic volume is observed. For more details, the reader is referred to the *supplementary material*.

3.3. Sintering

Fig. 1 illustrates the approach used for simulating the sintering process. Spherical single crystal nanoparticles (NPs) of three different radii $R = 2, 4$ and 6 nm are considered for the solid-phase sintering simulations. A bulk Al_2O_3 system, with $[11\bar{2}0]$, $[10\bar{1}0]$ and $[0001]$ in x , y and z directions of the simulation box, respectively, is created using the atomic simulation environment tool [37]. Spherical particles of different radii are cut out of the bulk system using AtomsK [38]. The simulation box is kept periodic in all three directions to keep the de-clustered atoms in the box. The minimum distance between the sphere surface and the ends of the simulation box is kept to be at least 25 \AA to avoid the influence of periodic images. The energy is minimised using the conjugate gradient and FIRE [39] algorithms to maximum force-norm value of $\approx 10^{-5} \text{ eV/\AA}$. The particle is initialised with a Gaussian velocity distribution corresponding to 60% of the melting temperature, followed by a microcanonical ensemble for 30 ps to stabilise the temperature of the system. Once

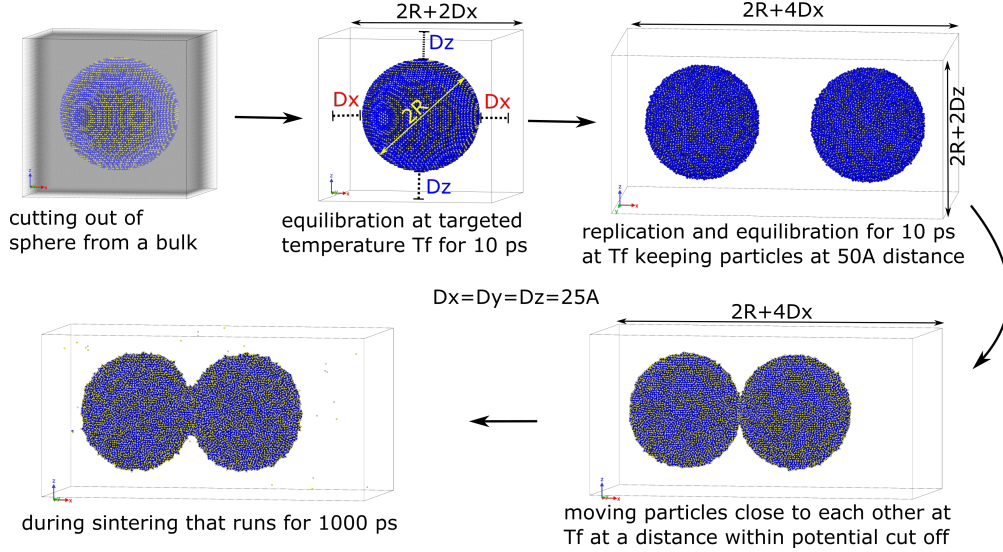


Figure 1: The simulation setup: A particle is cut out from bulk material (shown as semi-transparent), where $D_x = D_y = D_z = 25 \text{ \AA}$ is the smallest distance between particle and the surfaces. Al and O atoms are colored with blue and yellow, respectively. The particle is heated up to the target temperature T_f and thermalised at T_f for 10 ps each. It is then replicated and equilibrated at T_f . The particles are then brought together at a distance within the potential cut off and at T_f . Subsequently, the system is maintained at the T_f for 1 ns during which sintering can occur under favorable conditions.

the system is equilibrated at $0.3T_m$, it is subsequently heated up to the targeted sintering temperature in an canonical (NVT) ensemble for 10 ps. The NP is then thermalised at the target temperature for 10 ps. Subsequently, a replica of the particle is created, generating another particle at the same temperature and size, keeping a minimum gap of 50 \AA between them. The entire system is thermalised again at the targeted temperature by an NVT for 10 ps. The particles are subsequently brought close to each other so that the distance between them is less than the cut-off distance of those interatomic potentials that have such a cut-off. The temperature of the system is then kept at the targeted temperature in an NVT ensemble for 1 ns. Under favourable conditions, inter-particle diffusion takes place resulting in sintering of the two NPs at constant temperature.

3.4. Characterisation of sintering

To compare the performance of the four potentials in terms of sintering it is required to characterise and to quantify the time and temperature dependent sintering process. As a comparison of sintered particles is complex (e.g., in terms of geometry), we use altogether six different quantities to characterise and quantify sintering, with their evolution providing

an indication on the amount of sintering.

3.4.1. Shrinkage ratio The coalescence of two particles can be quantified by the shrinkage ratio S_f which is defined as:

$$S_f = 1 - \frac{d_{\text{COM}}}{(d_1 + d_2)/2}, \quad (14)$$

where d_1 and d_2 are particle sizes (diameters), and d_{COM} denotes the distance between the centres of mass of them. The latter is obtained as geometric mean of the atomic positions belonging to the particle under consideration. S_f is initially negative when NPs are detached, and zero when they are brought into contact. If sintering takes place, the particles move closer to each other resulting in an increase in S_f . When the two spheres are completely sintered, the centre-to-centre distance is ideally zero, resulting in S_f being one.

3.4.2. Surface area We note that during sintering, a reduction in surface area is to be expected: this reduction is driven by the movement of surface atoms which are more mobile than the atoms closer to the core of the particle. The transport of material results in reduction of surface area and thus a reduction of overall energy [40, 41]. To compute the surface area, we use the *construct surface-mesh modifier* in OVITO [42]. The algorithm constructs a surface mesh with Delaunay tetrahedralisation of the atomic points in conjunction with an appropriate probe sphere radius, where elements are removed that do not fit in the probe sphere. The remaining triangular faces of the tetrahedra defines a 2D boundary or surface of the defined domain. For more details, the reader is referred to [43]. The virtual probe spheres fill in the empty space between atomic points without spanning the atomic points. A smaller value gives more details of mesh, and a larger one smooths out the mesh. Three values for the probe radius (2, 4 and 6 Å) were tested. No difference was observed in the results for probe radii of 4 and 6 Å; hence a radius of 6 Å was chosen for the final analysis. The resulting surface area is then normalised by the initial surface area to facilitate comparison of different particle sizes and potentials.

3.4.3. Mean square displacement (MSD) The MSD defines the average displacement of all atoms in a system with respect to their original positions. It provides a good approximation of diffusion taking place during sintering at different temperatures and is defined as

$$\text{MSD}(t) = \langle |\mathbf{r}_i(t) - \mathbf{r}_i(0)|^2 \rangle, \quad (15)$$

where $\mathbf{r}_i(t)$ and $\mathbf{r}_i(0)$ are the current and initial positions of atom i , respectively.

3.4.4. Neck curvature The transport of surface atoms to reduce the overall surface area results in a reduction of curvature at the neck, i.e., the region where the two particles meet. The neck curvature hence provides a good estimate of the amount of sintering. In the case of

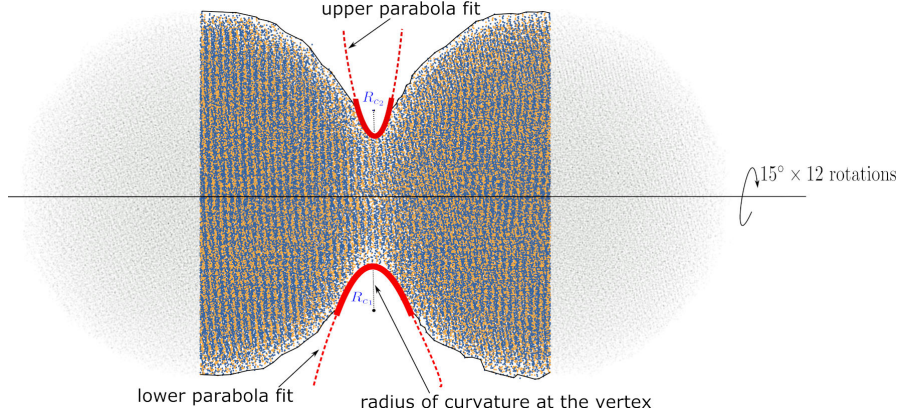


Figure 2: Calculation of neck curvature: Atoms projected onto a plane are shown as coloured points. From them the projected particle boundaries are identified (solid black line). Fitting parabolas to the regions with smallest diameter (red dashed line) allows to compute the radii of curvature, R_{c_1} and R_{c_2} . This is repeated for 12 different rotation angles.

completely sintered particles, the neck is completely eliminated, resulting in a value of 0 for the curvature. We compute the curvature as follows: 3D atomic coordinates are projected onto a plane whose normal is perpendicular to the centre-to-centre axis of the two particles. The boundaries of this region are obtained from spline fitting of the projected data, resulting in two curves that define the profile of the neck. Subsequently, the local minimum/maximum of the two curves are identified, to which second order parabolas ($y = ax^2 + bx + c$) are fitted and from which the curvature can be computed. This is repeated for rotations of 15° of the sample about the centre-to-centre axis of the two NPs, resulting in a total of 24 radii of curvatures for a given simulation snapshot. The mean radius of curvature \bar{R}_c is calculated as the arithmetic average of all values from which the mean neck curvature κ is obtained as $\kappa = 1/\bar{R}_c$. Fig. 2 provides a schematic diagram of the procedure.

3.4.5. Fraction of ions at the neck During the sintering process, the Al and O ions change their positions in the contact region, and this material transport reduces the curvature. The change in the geometry of the neck can then also be quantified by the fraction of ions forming the neck region. This is done via the following procedure: The atoms in the initial configuration are assigned an index (0 or 1) based on the NP they belong to. For each snapshot in time, the average index of the nearest neighbour atoms is computed, and those atoms with an averaged index between 0.9 and 1.1 are defined to constitute the neck region.

3.4.6. Norm of stretch tensor A disadvantage of MSD is that it may lead to erroneous results under the presence of rigid body motion, as will be evident by the results presented below. An alternative measure can be constructed by using displacements whilst accounting

for the immediate neighbourhood of individual atoms: we first construct the deformation gradient tensor using the displacement vectors of individual atoms. Using the polar decomposition $\mathbf{F}_i = \mathbf{U}_i \mathbf{R}_i$, we can decompose \mathbf{F}_i into the right stretch tensor, \mathbf{U}_i , and the rotation tensor, \mathbf{R}_i . Exploiting the orthogonality of \mathbf{R}_i , we obtain \mathbf{U}_i as:

$$\mathbf{U}_i = \sqrt{\mathbf{F}_i^T \mathbf{F}_i}, \quad (16)$$

and subsequently, the rotation tensor as

$$\mathbf{R}_i = \mathbf{F}_i \mathbf{U}_i^{-1} \quad (17)$$

The stretch tensor of individual atoms is subsequently averaged over the nearest neighbors as follows:

$$\bar{\mathbf{U}} = \frac{\sum \mathbf{U}_i V_i}{\sum V_i}, \quad (18)$$

where V_i is the atomic volume obtained via a Voronoi construction. For further analysis, we consider the square Euclidean norm of the averaged stretch tensor $\left(\|\bar{\mathbf{U}}\|^2\right)$ as the characteristic that quantifies sintering.

4. Results

4.1. Potential and material properties

Material properties such as lattice constants, cohesive energies, vacancy formation energies, elastic constants, surface energies and melting temperatures were calculated as described in Section 3 and the appendix, respectively. These properties, calculated with all four potentials along with the values from various experiments and density functional theory calculations are provided in Tab. 1. A graphical comparison of the range of properties is shown in Fig. 3. In the following, we treat values from experiments and DFT equivalently and refer to them collectively as experiments.

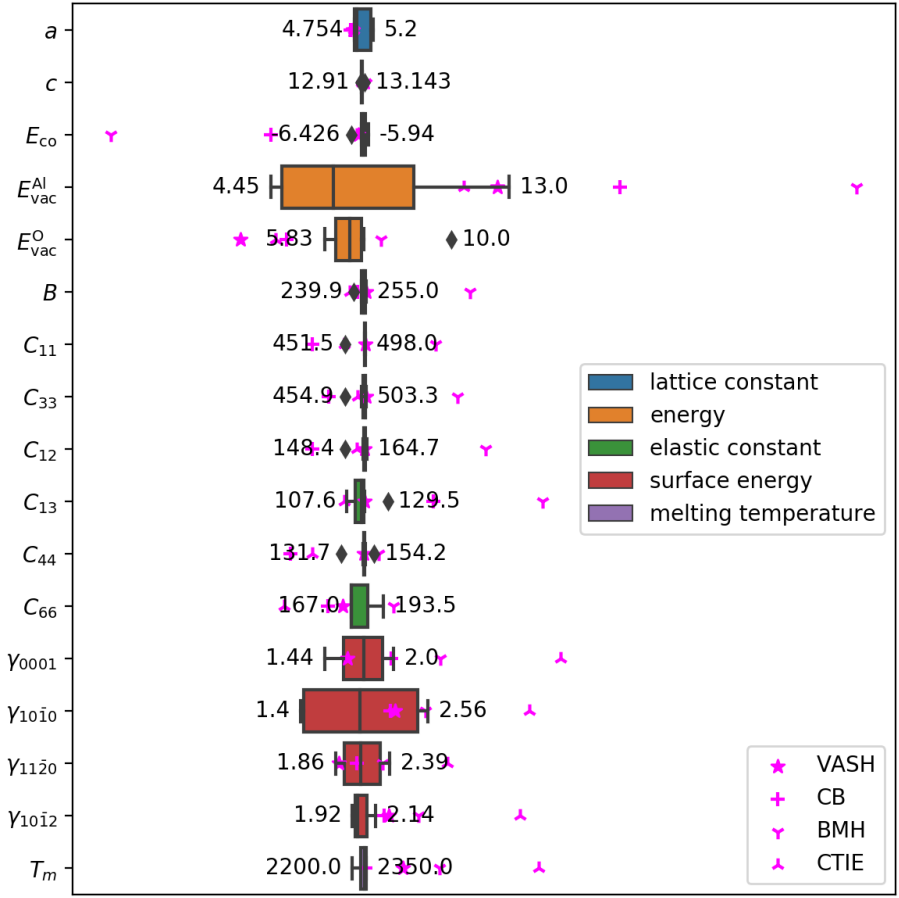


Figure 3: Boxplot of the properties of Al_2O_3 obtained from experiments together with our data obtained for the four potentials (pink markers). The coloured boxes show the quartiles and median of the data, the “whiskers” show the data extent, black diamonds are outliers. For plotting all data in the same plot, the data for each boxplot was normalised by the respective mean value; our data was normalised by the mean of the experimental and DFT values. For ease of readability, the values for C_{14} are not shown (cf. Tab. 1 instead).

Parameters	Experiment & DFT		Vashishta		Coulomb-Buckingham		BMH	CTI+EAM	
	value range	references	from [24]	our results	from [28]	our results	our results	from [26]	our results
a (Å)	4.754... 5.2	[44–51]		4.72	4.71, 4.7727 _[33]	4.68	4.74	5.13	4.74
c (Å)	12.91... 13.143	[46, 48, 50, 52, 53]		13.17	13.14, 12.99 _[33]	13.07	13.18		12.98
E_{co} (eV)	−6.426... − 5.94	[54–58]	−6.35	−6.35		−8.91	−13.56	−6.36	−6.39
E_{vac}^{Al} (eV)	4.45... 13	[47, 59–61]		12.56		16.96	25.46		11.36
E_{vac}^O (eV)	5.83... 10	[47, 59, 61–64]		3.07		4.57	7.68		4.23
B (GPa)	239.9... 255	[44, 45, 47, 50, 54]	253	247	258, 391.1 _[33]	255	377		236
C_{11} (GPa)	451.5... 498	[44, 45, 47, 49, 54, 65, 66]	523	476	714.5 _[33]	458	659	537	451
C_{33} (GPa)	454.9... 503.3	[44, 45, 47, 49, 54, 65, 66]	427	415	709.3 _[33]	490	712	509	483
C_{12} (GPa)	148.4... 164.7	[44, 45, 47, 49, 54, 65, 66]	147	155	327.5 _[33]	172	254	180	157
C_{13} (GPa)	107.6... 129.5	[44, 45, 47, 49, 54, 65, 66]	129	135	187.8 _[33]	124	213	106	106
C_{44} (GPa)	131.7... 154.2	[44, 45, 47, 49, 54, 66]	135	149	99.7 _[33]	117	157	130	112
C_{66} (GPa)	167... 193.5	[44, 45, 47, 54, 65]	174	160	193.5 _[33]	148	202	179	147
C_{14} (GPa)	−24... + 22.5	[47, 49, 54, 65, 66]	7.5	9	−42.2 _[33]	0.02	0	−30	−0.001
γ_{0001} (J/m ²)	1.44... 2.00	[35, 51, 67–71]		1.63 ^{Al}		1.98 ^{Al}	2.38 ^{Al}	2.67	3.36 ^{Al}
$\gamma_{10\bar{1}0}$ (J/m ²)	1.40... 2.56	[35, 67–69]		2.26 ^{Al-O}		2.22 ^{Al-O}	2.54 ^{Al-O}	1.28	3.49 ^{Al-O}
$\gamma_{11\bar{2}0}$ (J/m ²)	1.86... 2.39	[35, 51, 67–69, 71]		1.89 ^O		2.07 ^O	2.32 ^O	1.81	2.96 ^O
$\gamma_{10\bar{1}2}$ (J/m ²)	1.92... 2.14	[35, 67, 69]		2.26 ^{Al-O}		2.22 ^{Al-O}	2.54 ^{Al-O}	1.80	3.49 ^{Al-O}
T_m (K)	2200... 2350	[72–74]	2760	2740	2425 – 2475 _[75]	2340	3140		4200

Table 1: Summary of our obtained material properties in comparison to values reported in the literature. The superscripts Al , $Al - O$ and O of the surface energies denote the terminating atoms on the slab surfaces. A simple check ($C_{66} = (C_{11} - C_{12})/2$) for each potential provides an additional validation of elastic constants calculation.

For most properties, the values predicted by almost all interatomic potentials are well within or close to the range of values obtained from experiments (cf. Tab. 1). The notable exception is seemingly the BMH potential which predicts values for 0 K properties that are significantly higher than those obtained from experiments. Exceptions are also seen in the case of vacancy formation energy of Al; while VASH and CTIE predict values towards the higher values observed in experiments, values from CB and BMH are significantly beyond the range of experimental values. The latter two also predict significantly higher (numerically, lower) cohesive energy values than that observed from experiments. In case of the surface energies, we observe values that are by and large close to the range of data obtained from experiments. Only the CTIE is an exception here: energies for all the surfaces are significantly higher than that seen in experiments.

The predicted melting temperature values obtained via MD simulations with the four potentials show that only the CB potential predicts a value well within the range of experimental data. The values from all other potentials are significantly higher, with the highest value of 4200 K by the CTIE potential. To facilitate objective comparison of the sintering process with the different potentials, we use the homologous temperature of the corresponding potential.

In Fig. 3 we show the 25/75 percentile, median and total range of material parameters measured or calculated by various techniques. Outliers are detected based on 150% of the inter-quartile range. The figure shows that some of the obtained material properties exhibit significant scatter together with a strong skewness of the distribution. For example, the highest melting temperature (4200 K) is almost 210% more than the lowest melting temperature (2000 K) reported in experiments; the median of $E_{\text{vac}}^{\text{O}}$ is strongly shifted towards the left, and all of our computed values for this property are outside the 25/75 percentile range of the literature values. The literature values for the lattice constants, cohesive energy as well as most of the elastic properties don't show much variance. Looking at this figure, the best conformance with the experimental values for most of the properties is obtained with the CB potential.

4.2. Sintering

The results of the sintering simulations for each investigated temperature and particle size are shown as supplementary movies M1 to M3, with each movie comparing the prediction of all four potentials. Fig. 4 and 5 show the evolution of all investigated characteristics over time for all four potentials (indicated by the different line colours), for three different particle sizes (indicated by markers) and for different temperatures (sub-plots in columns).

Shrinkage ratio: Fig. 4a shows the evolution of the shrinkage ratio (S_f). For all four potentials, we generally observe an increase of S_f with time, particularly at higher

temperatures, implying that the two particles move closer to each other. However, the magnitude of this movement differs strongly from one potential to another, for all particle sizes and temperatures. At $T = 0.6 T_m$, for $R = 4$ nm and 6 nm, S_f remains negative or close to zero throughout the simulation, indicating that the two particles barely come into contact with each other. At this temperature, a non-negligible value of S_f is only observed for particles with $R = 2$ nm and potentials CTIE, BMH and VASH; while the former two display a steady increase in S_f , VASH shows an almost instantaneous increase to $\approx 5\%$ at the start which is then maintained throughout the simulation.

The evolution of S_f at $T = 0.7 T_m$ follows similar trends, however, for NPs with $R = 2$ nm, a non-negligible positive S_f is seen for all four potentials. While a steady increase over the entire simulation time and a value greater than 40% is observed for BMH, CB and CTIE, VASH displays an increase only within the first 0.2 ns and a saturation to significantly lower value of roughly 10%. Additionally, CTIE shows a S_f value of roughly 50% and 20% for $R = 4$ nm and 6 nm, respectively; for these particle radii, other potentials do not show any noticeable value of S_f .

Significantly different trends are seen at the higher temperature of $T = 0.8 T_m$. Both CB and BMH show very similar characteristics in the evolution of S_f over time. For the three particle sizes, S_f evolves towards higher values than at lower temperatures and attains values of 0.7, 0.4 and 0.2 after 1 ns, evidencing a trend of decreasing S_f with increasing particle size. In general, S_f with CTIE is higher than that predicted by other potentials. Very contrasting trends are seen for the VASH potential: Whilst the evolution for $R = 2$ nm follows that of CTIE, for $R = 4$ nm, S_f saturates to a value of 0.1 after 0.2 ns and remains negative for $R = 6$ nm.

Surface area: The evolution of overall surface area (A_f) of the NPs is shown in Fig. 4b. To enable easy comparison, the values are normalised w.r.t. the corresponding initial area before the start of the sintering process. Therefore, values should start at 1 and are expected to reduce during the simulation time if sintering proceeds favourably.

By and large, evolution of A_f displays trends similar to that observed for S_f : when the two NPs come close to each other, a decreasing surface area over time is generally observed (compare at $T = 0.6 T_m$: BMH, VASH and CTIE potentials and at $R = 2$ nm and $T = 0.7 T_m$: BMH, CB and CTIE). For cases where no sintering is expected (evidenced by zero shrinkage ratio), A_f remains close to unity.

Mean square displacement: The evolution of MSD over time is shown in Fig. 4c. The curves clearly show an increase in MSD over time, albeit with different amounts for different sample sizes and potentials. With increasing temperature, a significantly higher MSD is observed, indicating the propensity for increased diffusion at higher temperatures. However, the trends do not complement those observed with S_f and A_f . For example, the MSD for

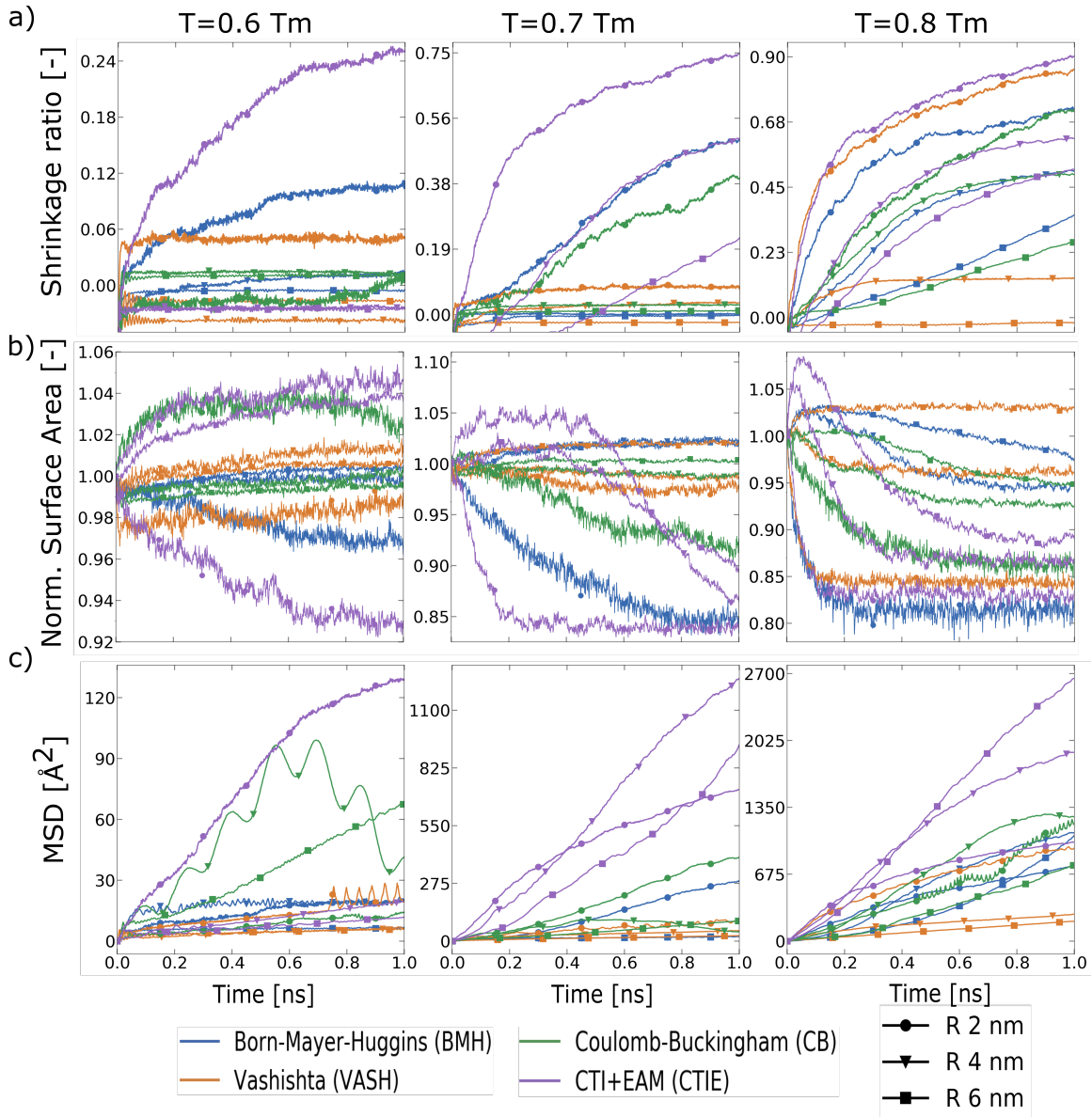


Figure 4: Evolution of the first three global quantities: a) shrinkage ratio, b) normalised surface area, and c) MSD. The left, middle and right column are for 60%, 70% and 80% of melting temperatures. Markers are shown at every 20 data points (= every 2 ps).

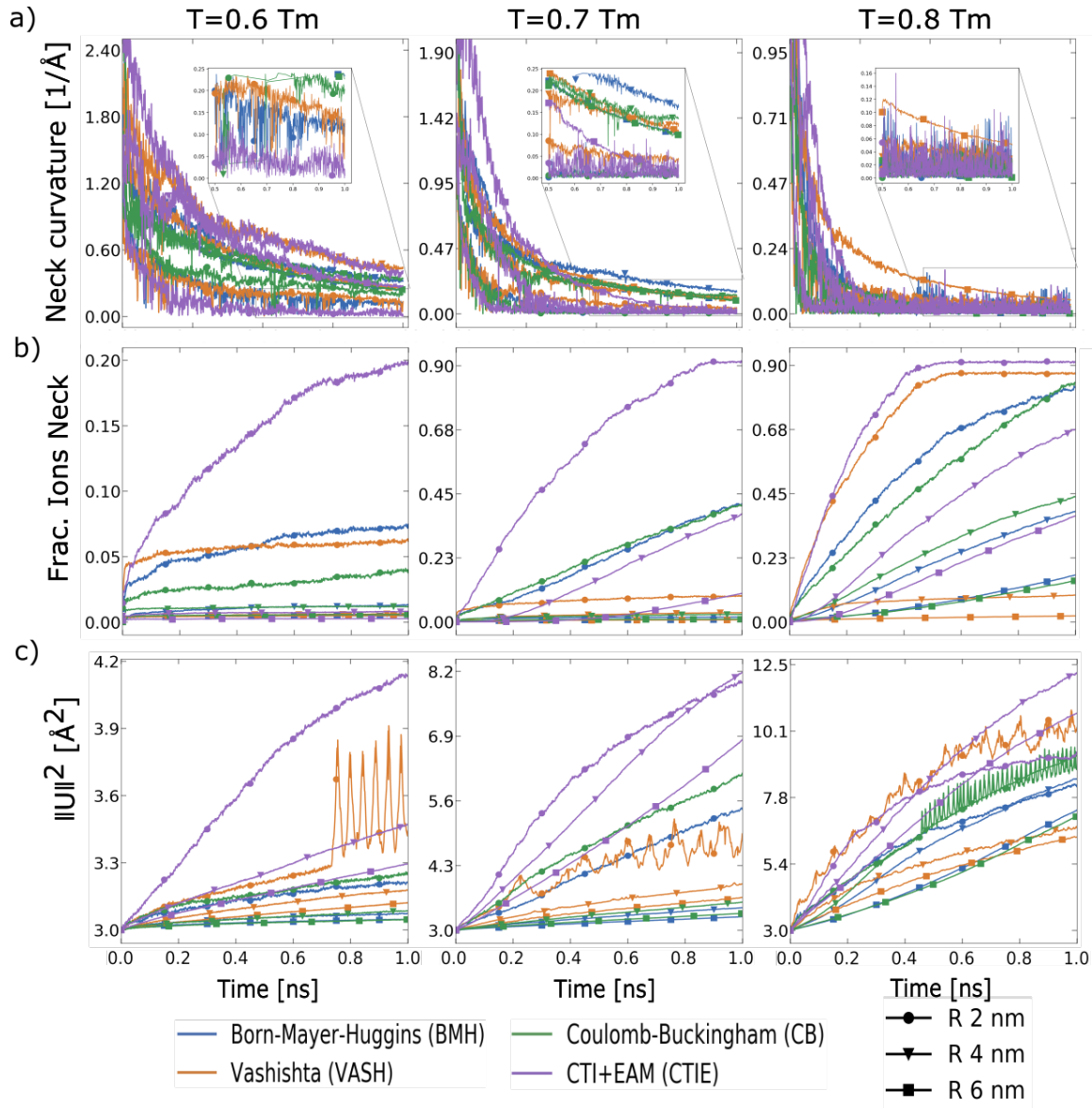


Figure 5: Evolution of the last three global quantities: a) curvature at the neck, b) fraction of ions at the neck, c) norm of the stretch tensor. The left, middle and right column are for 60%, 70% and 80% of melting temperatures. Markers are shown at every 20 data points (= every 2 ps).

CTIE at $T = 0.7 T_m$ is greater than the MSD for all other potentials and particle sizes, which contradicts the trends observed with S_f . This can be observed at $T = 0.6 T_m$ and $T = 0.7 T_m$ as well. Furthermore, the evolution of MSD with the CB potential at $T = 0.6 T_m$ shows non-monotonic evolution with periodic crests and troughs, indicating artifacts associated with the superposition of rigid body motion.

Neck curvature: The change in the neck curvature κ with time is shown in Fig. 5a and, as expected, decreases with time. A value of zero indicates a complete removal of the neck region. The initial value of κ for larger particles are higher than that of the smaller particles, and at the same time, the initial change in the curvature for $R = 2$ nm is faster than that for $R = 4$ nm and $R = 6$ nm for all temperatures. Generally, no unexpected trends are observed and the evolution is consistent with the trends observed for S_f .

Fraction of ions at the neck: The change in the accumulated fraction of ions at the neck, N_f^i , is shown in Fig. 5b. The observed trends here align well with those seen in the shrinkage ratio. With increasing temperature, N_f^i reaches values as high as 0.9, indicating that almost the entire system of two particles is now classified as the neck region. Such a scenario occurs when the two particles have completely sintered and remixing of atoms from the two particles has taken place. At lower temperatures N_f^i reaches substantially lower values; the only exception seemingly is for $R = 2$ nm with the CTIE potential at $T = 0.7 T_m$, where a value of more than 0.9 is reached.

Norm of stretch tensor: Fig. 5c shows that the evolution of $|\mathbf{U}|^2$ starts at a value of 3 since the initial stretch tensor is an identity tensor. The square of the norm is used here to facilitate comparison with MSD. Here, it is evident that there are differences between the evolution of $|\mathbf{U}|^2$ and MSD: at $T = 0.8 T_m$, the MSD after 1 ns for VASH is significantly lower than other potentials for $R = 4$ nm and 6 nm, whereas the $|\mathbf{U}|^2$ values are very similar to those from BMH and CB for $R = 6$ nm. Furthermore, the non-monotonic evolution with periodic crests and troughs seen with the CB potential at $T = 0.6 T_m$ vanishes in the evolution of $|\mathbf{U}|^2$. However, for the VASH potential, the evolution of $|\mathbf{U}|^2$ shows fluctuations from the mean at all temperatures. These fluctuations, also visible with the evolution of MSD.

5. Discussion

We study the different formulations and parameterisation of four potentials and investigate how they result in different amounts of sintering for three different temperatures and particle sizes. In the current work, six measures are used to characterise sintering and to quantify the process. It is hence important to discuss the pros and cons of these measures, since not all measures are able to quantify the sintering process to the same extent.

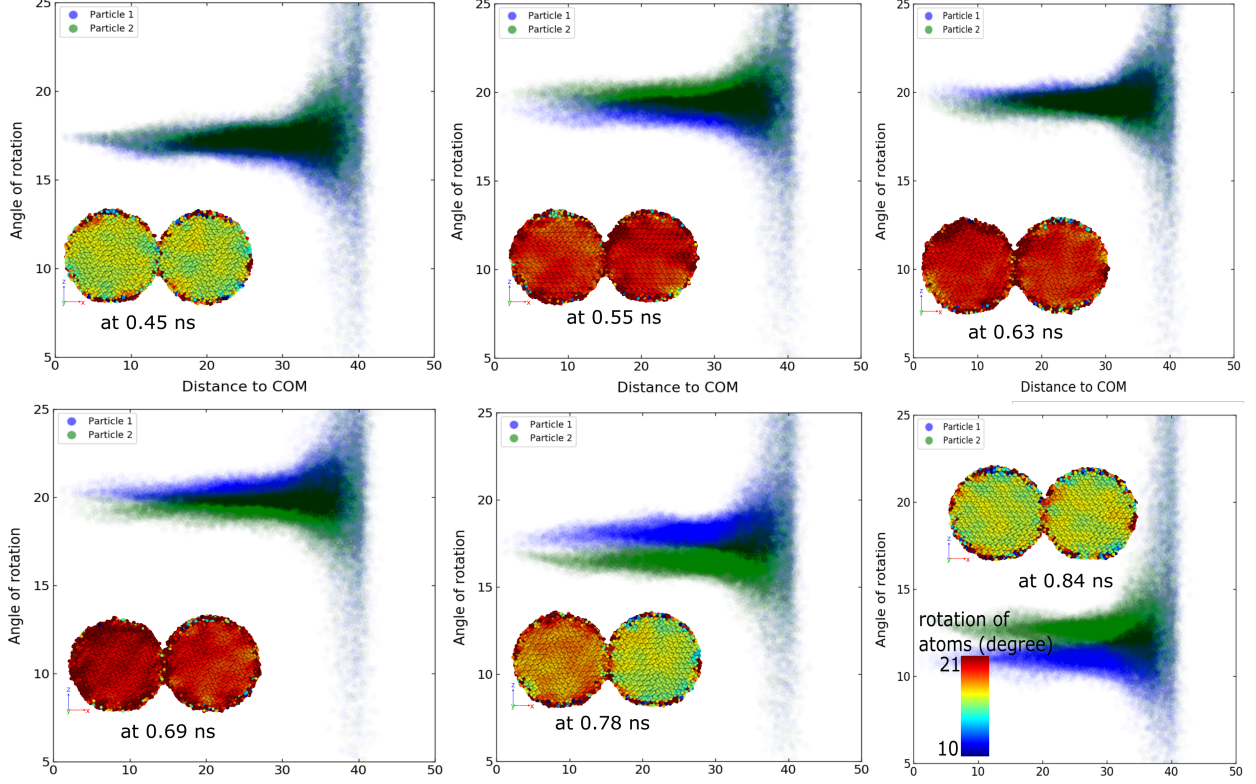


Figure 6: Rotation distribution of atoms for two NPs with the distance from centre of masses of the corresponding particles is plotted. The insets are snapshots of atomic structure contoured with the amount of rotation at various simulation times with respect to their positions at time zero for potential CB and radius $R = 4$ nm at $T = 0.6 T_m$. The distribution and the snapshots are chosen at the simulations times when MSD changes its evolution path (see Fig. 4c).

In particular, it is visible that the MSD is prone to influences from rigid body motion, resulting in a non-monotonic evolution over time as seen for instance with CB for $R = 4$ nm and $T = 0.6 T_m$. We note that the simulations are performed with periodic boundary conditions and the MSD is calculated using only the atoms participating in the sintering process, i.e. atoms that detach themselves from the main particle are neglected. To understand the non-monotonic evolution in MSD, we investigate the rigid body rotation of the two particles, see Fig. 6. This is done by using the polar decomposition of the deformation gradient $\mathbf{F} = \mathbf{R}\mathbf{U}$ and expressing the rotation tensor \mathbf{R} in terms of an angle that denotes the rotation of an individual atom from the initial configuration. It is evident that the crests and troughs in the evolution of MSD correspond to significant changes in the rotation of the two particles. This non-monotonic evolution is eliminated when the rotational part is removed from the displacement, as is the case with the stretch tensor $|\mathbf{U}|^2$

Interpretation of the colour code:

- 0: no substantial change relative to the initial configuration
- 1: minimal formation of the neck region
- 2: significant progress of the neck region
- 2.5: sintering of the two particles without remixing of ions
- 3: sintering with complete remixing.

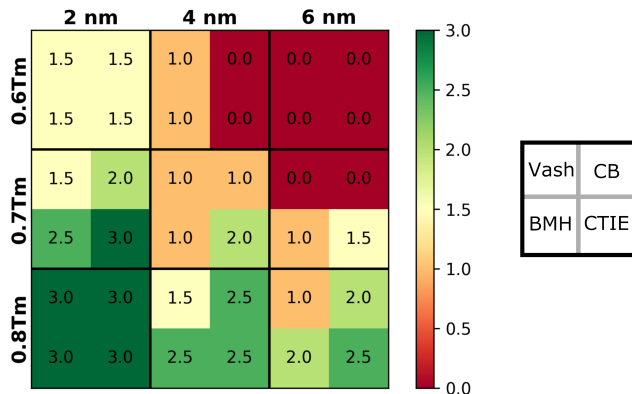


Figure 7: Quantification of the amount of sintering by “visual inspection” for all investigated potentials, particle sizes and temperatures.

(cf. Fig. 5c). MSD, as a quantifying measure of the sintering process, must hence be used with caution. Indeed, we strongly suggest the use of $|\mathbf{U}|^2$, which essentially encapsulates MSD whilst accounting for the immediate neighbourhood of individual atoms.

All six measures aim to quantify the same sintering process. Therefore, they should be able answer the questions a) which of these quantities give a definitive indication on the amount of sintering?, and b) what numerical value of the said quantity indicates complete sintering? In principle all six measures should be consistent with each other if they perform equally well. However, significant discrepancies can be observed in the evolution of these quantities. For instance, MSD (and also $|\mathbf{U}|^2$) for $R = 4$ nm and $R = 6$ nm at $T = 0.8T_m$ for CTIE is higher than that for all other potentials and particle sizes. This trend is not observed with other quantities, such as the fraction of ions in the neck, F_{ion} , or the shrinkage ratio, S_f . Also, it is not completely evident from the quantities themselves if we indeed have complete sintering or not.

How strongly do the six sintering measures correlate with our expectation and experience? Fig. 7 provides a quantification of the amount of sintering obtained via visual inspection. The scale of 0–3 indicates no substantial change in the initial configuration (0) to complete sintering (3).

The normalised surface area A_f and the neck curvature are perhaps the most intuitive measures to set numerical thresholds that indicate complete sintering. In the ideal case of two particles being completely sintered and become one sphere, the normalised surface area should decrease to a value of approx. 0.79, and the neck curvature to zero. However, the discrete nature of the system and the approximations used in the two algorithms can result in large fluctuations due to small perturbations, making these quantities sensitive and error-prone.

The shrinkage ratio S_f and the fraction of ions in the neck F_{ion} are less intuitive, but seemingly the more robust measures to quantify sintering. In the ideal case of complete

sintering, S_f should evolve to a value of 1. In the way how we define the neck region, complete sintering would involve remixing of atoms from the two original NPs resulting in the entire sintered particle being classified as neck leading to a value of 1 for F_{ion} . In practice, however, values of approximately 0.7 and 0.8 for S_f and F_{ion} , respectively, are seemingly sufficient to indicate complete sintering, while values of 0.5 and 0.35, respectively, indicate partial sintering, i.e., two particles have become a single particle, albeit without significant remixing of ions from the two particles. The latter case is merely a question of kinetics and would result in the former case with increased simulation time. We note, nonetheless, that these numerical values have no physical meaning and are mere observations from our simulations.

A focal point of the current work is the comparison of interatomic potentials for the simulation of sintering. A key component of atomistic simulations is the reliability and applicability of interatomic potentials. Empirical potentials, such as those used in the current work, are usually derived by fitting a functional to certain properties of the material under consideration. All four potentials used in the current work make use of lattice constants and the bulk modulus of alumina in their fitting procedure. Cohesive energy is used additionally for the parameterisation of CTIE and VASH potentials. In this regard, it is unsurprising that the values of these properties fall well within the range of values obtained from experiments (see Fig. 3). All other material properties listed in table 1, including the vacancy formation energies and the surface energies, are predicted values and differ significantly from one potential to another.

The decision on which interatomic potential to use is generally taken based on the accuracy of the predicted material properties, which are usually not a part of the fitting procedure. The two main properties of interest in the sintering process are the surface energies and the vacancy formation energies. The former is of lesser relevance in the current work due to the usage of spherical particles. Nevertheless, we note that all potentials but for BMH, predict surface energies within the range determined by experiments.

The values of the vacancy formation energies – both Al and O-site vacancy energies – predicted by the four potentials are, however, significantly different from one another. While the values of the O-site vacancy energies are very close to experimental values, those of Al-site vacancy energies predicted by CB and BMH potentials are significantly higher than experimental values. In general, the following trend is observed in the predicted values of the vacancy formation energies: $\text{VASH} < \text{CTIE} < \text{CB} < \text{BMH}$, with the lowest values predicted by the VASH potential.

Given the proximity in the values of most material properties to those obtained from experiments, and the low vacancy formation energies, we should expect the best prediction of the sintering process with the VASH potential. However, comparison of the amount of sintering (see Fig. 7) shows completely contradictory results with the least amount of sintering with VASH and furthermore, a near absence of sintering of particles of larger size

($R = 4$ nm and $R = 6$ nm) even at $T = 0.7 T_m$ and $T = 0.8 T_m$. By contrast, all other potentials show an increased amount of sintering at $T = 0.8 T_m$. The reduced progress in sintering for the highest particle radius of $R = 6$ nm reflects the slower kinetics, and is likely to result in a completely sintered state with increased time. With the VASH potential, however, an increased simulation time is unlikely to yield any changes as is evident in the characteristics presented in Fig. 4 and Fig. 5.

It hence follows that the origin of these differences lies in the functional form and treatment of the individual potentials. The VASH potential includes both two-body and three-body interactions, the latter being applied only to triplets of atoms. The former, which includes Coulomb interactions, is truncated at $r_{\text{cut}} = 6 \text{ \AA}$ [24]. Such truncation is unlikely to have an effect on periodic systems as is evident in the accuracy of the material properties predicted by the potential. In the presence of free surfaces, such truncation results in significant discrepancies like pseudo size effects observed in the sintering of larger particles at higher temperatures.

As pointed out in section 2, the formulations of the BMH and CB potentials are effectively identical in the manner they are used in the current work. The BMH potential is indeed a re-parameterisation of the CB potential [23]. The key difference between the two potentials is in the effective charges (Z_i) used for Al and O ions: in the BMH potential charge values close to those in pure oxide systems [76] are used. This difference in charges has a significant effect on the material properties predicted by the two potentials, but has apparently no effect on kinetics of the sintering process. Evidently, for all particle sizes and temperatures considered in the current study, the amount of sintering predicted by the two potentials is almost the same.

Of the four potentials, the CTIE potential results in the highest kinetics of the sintering process. A plausible reason for this is the charge equilibration performed in this potential. In the presence of a heterogeneous electrostatic environment, as e.g. interfaces and free surfaces, ions are likely to have varying charges depending on their local environment. The ability to perform charge equilibration allows for different charges for different ions, depending on their local environment, which we believe is the reason for improved kinetics with the CTIE potential. A further improvement in the simulations can be introduced by activating dynamic charge transfer in the CTIE potential since this is known to enhance atomic diffusion in surface regions of nanoparticles [77].

We hence summarize that accurate treatment of Coulomb effects, together with correct effective charges of the ions, are important for effective prediction of sintering in atomistic simulations of alumina. The usage of effective charges can result in improved kinetics of the sintering process. Truncation of Coulomb effects, however, is more critical and can result in spurious size effects during sintering.

6. Conclusions

In this study, we perform atomistic simulations of sintering and compare four interatomic potentials for alumina. The four potentials – VASH, CB, BMH and CTIE – differ in the formulation as well as in their treatment of Coulomb interactions and individual charges. The potentials are first compared in terms of their ability to predict fundamental material properties. Three different particle sizes and temperatures are used to study the sintering process, which is subsequently characterised using six different quantities. The findings of the study can be summarised as follows:

- All four potentials predict lattice constants that are well within the range of experimental values. Only VASH and CTIE predict cohesive energies that are close to experiments. Both CB and BMH predict significantly higher values of cohesive energy
- The values of most elastic constants are significantly higher with the BMH potential. With the other three potentials, most of the values are very close to those obtained from experiments.
- The surface energy values predicted by the CTIE potential are significantly higher than the experimental values. All other potentials predict values well within the range determined by experiments.
- The vacancy formation energy values of both Al and O sites follows the following trend: $VASH < CTIE < CB < BMH$.
- All potentials show an increasing amount of sintering with increasing temperature for the nanoparticle with $R = 2$ nm, with complete sintering observed at $T = 0.8 T_m$.
- Very little or no sintering is observed for the largest particle size of $R = 6$ nm at temperatures $T = 0.7 T_m$ and below.
- Except for the VASH potential, all other potentials predict significant amount of sintering at $T = 0.8 T_m$ for all particle sizes.
- For the quantification of the sintering process, the use of $|\mathbf{U}|^2$ is recommended over MSD, since the latter is particularly prone to influences of rigid body motion of the particles.
- The shrinkage ratio (S_f) and fraction of ions in the neck (F_{ion}) provide the best quantification of the sintering process. Numerical values of 0.7 and 0.8 for S_f and F_{ion} , respectively, indicate complete sintering.
- The abrupt cutoff of Coulomb interactions is deemed as the reason for the spurious behaviour of the VASH potential, which shows almost no sintering for particle sizes above $R = 2$ nm, even at the high temperature of $T = 0.8 T_m$.
- The CTIE potential predicts the highest amount of sintering amongst all potentials compared in the current work. The increased kinetics is attributed to the ability to perform charge equilibration within the potential.

Acknowledgments

The authors thank Prof. H. Riedel for fruitful discussions. This work is supported by the German Research Foundation (DFG) within the framework of the Collaborative Research Center SFB 920 Project-ID169148856 “Multi-Functional Filters for Metal Melt Filtration – A Contribution toward Zero Defect Materials”, subproject B04. The authors gratefully acknowledge (i) computing time granted on the high-performance compute cluster operated by the University Computing Center (URZ) of the TU Bergakademie Freiberg and (ii) computing time granted through JARA on the supercomputer JUQUEEN [78] at Forschungszentrum Jülich.

Data availability

Postprocessed datasets and chosen visualisation scripts can be obtained from gitlab XYZ, raw data and simulation/analysis code is made available upon reasonable request.

References

- [1] Vivek T Rathod, Jayanth S Kumar, and Anjana Jain. Polymer and ceramic nanocomposites for aerospace applications. *Applied Nanoscience*, 7(8):519–548, 2017.
- [2] Amit Bhatnagar, Eva Kumar, and Mika Sillanpää. Nitrate removal from water by nano-alumina: Characterization and sorption studies. *Chemical Engineering Journal*, 163(3):317–323, 2010.
- [3] Sandeep Sarkar, Sibdas Bandyopadhyay, André Larbot, and Sophie Cerneaux. New clay–alumina porous capillary supports for filtration application. *Journal of Membrane Science*, 392:130–136, 2012.
- [4] Veeranna Sridhara and Lakshmi Narayan Satapathy. Al₂O₃-based nanofluids: a review. *Nanoscale Research Letters*, 6(1):456, 2011.
- [5] I Mohammed Sadiq, Basudev Chowdhury, Natarajan Chandrasekaran, and Amitava Mukherjee. Antimicrobial sensitivity of escherichia coli to alumina nanoparticles. *Nanomedicine: Nanotechnology, Biology and Medicine*, 5(3):282–286, 2009.
- [6] Lillian C Becker, Ivan Boyer, Wilma F Bergfeld, Donald V Belsito, Ronald A Hill, Curtis D Klaassen, Daniel C Liebler, James G Marks Jr, Ronald C Shank, Thomas J Slaga, et al. Safety assessment of alumina and aluminum hydroxide as used in cosmetics. *International Journal of Toxicology*, 35(3_suppl):16S–33S, 2016.
- [7] Mehdi Mahmoudian, Ahmad Poursattar Marjani, Rezgar Hasanzadeh, Ehsan Nozad, Sajjad Mamaghani Shishavan, and Haniyeh Mohamadi. Effect of in-situ modification of α -alumina nanoparticles on mechanical properties of poly (methyl methacrylate)-based

- nanocomposites for biomedical applications. *Materials Research Express*, 6(10):105410, 2019.
- [8] Jérôme Chevalier and Laurent Gremillard. Ceramics for medical applications: A picture for the next 20 years. *Journal of the European Ceramic Society*, 29(7):1245–1255, 2009.
- [9] SF Hulbert. The use of alumina and zirconia in surgical implants. *Advanced Series in Ceramics*, 1:25–40, 1993.
- [10] Rajaa Benzaid, Jerome Chevalier, Malika Saâdaoui, Gilbert Fantozzi, Masahiro Nawa, Luis Antonio Diaz, and Ramon Torrecillas. Fracture toughness, strength and slow crack growth in a ceria stabilized zirconia–alumina nanocomposite for medical applications. *Biomaterials*, 29(27):3636–3641, 2008.
- [11] Matjaz Valant, Uroš Luin, Mattia Fanetti, Andraž Mavrič, Kateryna Vyshniakova, Zdravko Siketić, and Mitjan Kalin. Fully transparent nanocomposite coating with an amorphous alumina matrix and exceptional wear and scratch resistance. *Advanced Functional Materials*, 26(24):4362–4369, 2016.
- [12] Qiong He, Dongyun Zheng, and Shengshui Hu. Development and application of a nano-alumina based nitric oxide sensor. *Microchimica Acta*, 164(3-4):459–464, 2009.
- [13] Barbara Kasprzyk-Hordern. Chemistry of alumina, reactions in aqueous solution and its application in water treatment. *Advances in Colloid and Interface Science*, 110(1-2): 19–48, 2004.
- [14] Suk-Joong L Kang. *Sintering: densification, grain growth and microstructure*. Elsevier, 2004.
- [15] Randall M German. Computer modeling of sintering processes. *International Journal of Powder Metallurgy*, 38(2):48–66, 2002.
- [16] Diana Farkas. Atomistic simulations of metallic microstructures. *Current Opinion in Solid State and Materials Science*, 17(6):284–297, 2013.
- [17] Wilfried Wunderlich. The atomistic structure of metal/ceramic interfaces is the key issue for developing better properties. *Metals*, 4(3):410–427, 2014.
- [18] Aruna Prakash and Erik Bitzek. Idealized vs. realistic microstructures: An atomistic simulation case study on γ/γ' microstructures. *Materials*, 10(1):88, 2017.
- [19] Jyotirmoy Nandy, Natraj Yedla, Pradeep Gupta, Hrushikesh Sarangi, and Seshadev Sahoo. Sintering of AlSi₁₀Mg particles in direct metal laser sintering process: A molecular dynamics simulation study. *Materials Chemistry and Physics*, 236:121803, 2019.
- [20] Pengxiang Song and Dongsheng Wen. Molecular dynamics simulation of the sintering of metallic nanoparticles. *Journal of Nanoparticle Research*, 12(3):823–829, 2010.

- [21] Vishal N Koparde and Peter T Cummings. Molecular dynamics simulation of titanium dioxide nanoparticle sintering. *The Journal of Physical Chemistry B*, 109(51):24280–24287, 2005.
- [22] Jiri Houska. Pathway for a low-temperature deposition of $\alpha - \text{Al}_2\text{O}_3$: A molecular dynamics study. *Surface and Coatings Technology*, 235:333–341, 2013.
- [23] M Bouhadja, N Jakse, and A Pasturel. Structural and dynamic properties of calcium aluminosilicate melts: A molecular dynamics study. *The Journal of Chemical Physics*, 138(22):224510, 2013.
- [24] Priya Vashishta, Rajiv K Kalia, Aiichiro Nakano, and José Pedro Rino. Interaction potentials for alumina and molecular dynamics simulations of amorphous and liquid alumina. *Journal of Applied Physics*, 103(8):083504, 2008.
- [25] Tao Liang, Yun Kyung Shin, Yu-Ting Cheng, Dundar E Yilmaz, Karthik Guda Vishnu, Osvalds Verners, Chenyu Zou, Simon R Phillpot, Susan B Sinnott, and Adri CT Van Duin. Reactive potentials for advanced atomistic simulations. *Annual Review of Materials Research*, 43:109–129, 2013.
- [26] FH Streitz and JW Mintmire. Electrostatic potentials for metal-oxide surfaces and interfaces. *Physical Review B*, 50(16):11996, 1994.
- [27] Anthony K Rappe and William A Goddard III. Charge equilibration for molecular dynamics simulations. *The Journal of Physical Chemistry*, 95(8):3358–3363, 1991.
- [28] Masanori Matsui. Molecular dynamics study of the structures and bulk moduli of crystals in the system $\text{CaO} - \text{MgO} - \text{Al}_2\text{O}_3 - \text{SiO}_2$. *Physics and Chemistry of Minerals*, 23(6):345–353, 1996.
- [29] Mattia Biesuz, Gianmarco Taveri, Andrew I Duff, Eugene Olevsky, Degui Zhu, Chunfeng Hu, and Salvatore Grasso. A theoretical analysis of cold sintering. *Advances in Applied Ceramics*, 119(2):75–89, 2020.
- [30] Salvatore Grasso, Mattia Biesuz, Luca Zoli, Gianmarco Taveri, Andrew I Duff, Daoyao Ke, Anna Jiang, and Michael J Reece. A review of cold sintering processes. *Advances in Applied Ceramics*, pages 1–29, 2020.
- [31] Cekdar Vakifahmetoglu and Levent Karacasulu. Cold sintering of ceramics and glasses: A review. *Current Opinion in Solid State and Materials Science*, page 100807, 2020.
- [32] Dnyansingh Bacorisen, Roger Smith, JA Ball, RW Grimes, BP Uberuaga, KE Sickafus, and WT Rankin. Molecular dynamics modelling of radiation damage in normal, partly inverse and inverse spinels. *Nuclear Instruments and Methods in Physics Research Section B: Beam Interactions with Materials and Atoms*, 250(1-2):36–45, 2006.
- [33] Jizhong Sun, T Stirner, WE Hagston, A Leyland, and A Matthews. A simple transferable interatomic potential model for binary oxides applied to bulk $\alpha - \text{Al}_2\text{O}_3$ and the (0001) $\alpha - \text{Al}_2\text{O}_3$ surface. *Journal of Crystal Growth*, 290(1):235–240, 2006.

- [34] Vo Van Hoang and Suhk Kun Oh. Simulation of structural properties and structural transformation of amorphous Al_2O_3 . *Physica B: Condensed Matter*, 352(1-4):73–85, 2004.
- [35] XW Zhou, HNG Wadley, J-S Filhol, and MN Neurock. Modified charge transfer–embedded atom method potential for metal/metal oxide systems. *Physical Review B*, 69(3):035402, 2004.
- [36] S. Plimpton. Fast parallel algorithms for short-range molecular dynamics. *Journal of Computational Physics*, 117(1):1–19, 1995.
- [37] Ask Hjorth Larsen, Jens Jørgen Mortensen, Jakob Blomqvist, Ivano E Castelli, Rune Christensen, Marcin Dułak, Jesper Friis, Michael N Groves, Bjørk Hammer, Cory Hargus, et al. The atomic simulation environment—a python library for working with atoms. *Journal of Physics: Condensed Matter*, 29(27):273002, 2017.
- [38] Pierre Hirel. AtomsK: a tool for manipulating and converting atomic data files. *Computer Physics Communications*, 197:212–219, 2015.
- [39] Julien Guérolé, Wolfram G Nöhring, Aviral Vaid, Frédéric Houllé, Zhuocheng Xie, Aruna Prakash, and Erik Bitzek. Assessment and optimization of the fast inertial relaxation engine (fire) for energy minimization in atomistic simulations and its implementation in lammmps. *Computational Materials Science*, 175:109584, 2020.
- [40] JP Jernot, M Coster, and JL Chermant. Model of variation of the specific surface area during sintering. *Powder Technology*, 30(1):21–29, 1981.
- [41] Randall M German. Sintering trajectories: description on how density, surface area, and grain size change. *Jom*, 68(3):878–884, 2016.
- [42] Alexander Stukowski. Visualization and analysis of atomistic simulation data with ovito—the open visualization tool. *Modelling and Simulation in Materials Science and Engineering*, 18(1):015012, 2009.
- [43] Alexander Stukowski. Computational analysis methods in atomistic modeling of crystals. *Jom*, 66(3):399–407, 2014.
- [44] David R Lide. *CRC handbook of chemistry and physics*, volume 85. CRC press, 2004.
- [45] Samsonov Gv. The oxide handbook. *IFI/Plenum Data Corporation, New York, 1982 p*, 206, 1982.
- [46] Nobuo Ishizawa, Tsutomu Miyata, Ichiro Minato, F Marumo, and S Iwai. A structural investigation of $\alpha\text{-Al}_2\text{O}_3$ at 2170 k. *Acta Crystallographica Section B: Structural Crystallography and Crystal Chemistry*, 36(2):228–230, 1980.
- [47] NDM Hine, K Frensch, WMC Foulkes, and MW Finnis. Supercell size scaling of density functional theory formation energies of charged defects. *Physical Review B*, 79(2):024112, 2009.

- [48] WE Lee and KPD Lagerlof. Structural and electron diffraction data for sapphire ($\alpha - \text{Al}_2\text{O}_3$). *Journal of Electron Microscopy Technique*, 2(3):247–258, 1985.
- [49] Shunli Shang, Yi Wang, and Zi-Kui Liu. First-principles elastic constants of α - and $\theta - \text{Al}_2\text{O}_3$. *Applied Physics Letters*, 90(10):101909, 2007.
- [50] Yu Liu, Yuanchun Huang, Zhengbing Xiao, Chuge Yang, and Xianwei Reng. First principles calculations of formation energies and elastic constants of inclusions $\alpha - \text{Al}_2\text{O}_3$, MgO and AlN in aluminum alloy. *International Journal of Modern Physics B*, 30(16):1650085, 2016.
- [51] Asma Tougeriti, Christophe Methivier, Sylvain Cristol, Frederik Tielens, Michel Che, and Xavier Carrier. Structure of clean and hydrated $\alpha - \text{Al}_2\text{O}_3$ (1 $\bar{1}$ 02) surfaces: implication on surface charge. *Physical Chemistry Chemical Physics*, 13(14):6531–6543, 2011.
- [52] J Lewis, D Schwarzenbach, and HD Flack. Electric field gradients and charge density in corundum, $\alpha - \text{Al}_2\text{O}_3$. *Acta Crystallographica Section A: Crystal Physics, Diffraction, Theoretical and General Crystallography*, 38(5):733–739, 1982.
- [53] Darwin P Sigumonrong, Denis Music, and Jochen M Schneider. Efficient supercell design for surface and interface calculations of hexagonal phases: $\alpha - \text{Al}_2\text{O}_3$ case study. *Computational Materials Science*, 50(3):1197–1201, 2011.
- [54] JH Gieske and GR Barsch. Pressure dependence of the elastic constants of single crystalline aluminum oxide. *Physica Status Solidi (b)*, 29(1):121–131, 1968.
- [55] Berit Hinnemann and Emily A Carter. Adsorption of al, o, hf, y, pt, and s atoms on $\alpha - \text{Al}_2\text{O}_3$ (0001). *The Journal of Physical Chemistry C*, 111(19):7105–7126, 2007.
- [56] C Rohmann, JB Metson, and H Idriss. DFT study of carbon monoxide adsorption on $\alpha - \text{Al}_2\text{O}_3$ (0001). *Surface Science*, 605(17-18):1694–1703, 2011.
- [57] Saman Alavi, Dan C Sorescu, and Donald L Thompson. Adsorption of hcl on single-crystal $\alpha - \text{Al}_2\text{O}_3$ (0001) surface: A DFT study. *The Journal of Physical Chemistry B*, 107(1):186–195, 2003.
- [58] Florian Janetzko, Robert A Evarestov, Thomas Bredow, and Karl Jug. First-principles periodic and semiempirical cyclic cluster calculations for single oxygen vacancies in crystalline Al_2O_3 . *Physica Status Solidi (b)*, 241(5):1032–1040, 2004.
- [59] Katsuyuki Matsunaga, Tomohito Tanaka, Takahisa Yamamoto, and Yuichi Ikuhara. First-principles calculations of intrinsic defects in Al_2O_3 . *Physical Review B*, 68(8):085110, 2003.
- [60] SK Mohapatra and FA Kröger. The dominant type of atomic disorder in $\alpha - \text{Al}_2\text{O}_3$. *Journal of the American Ceramic Society*, 61(3-4):106–109, 1978.
- [61] Javier Carrasco, José RB Gomes, and Francesc Illas. Theoretical study of bulk and

- surface oxygen and aluminum vacancies in $\alpha - \text{Al}_2\text{O}_3$. *Physical Review B*, 69(6):064116, 2004.
- [62] Isao Tanaka, Kazuyoshi Tatsumi, Masanobu Nakano, Hirohiko Adachi, and Fumiyasu Oba. First-principles calculations of anion vacancies in oxides and nitrides. *Journal of the American Ceramic Society*, 85(1):68–74, 2002.
- [63] Yong-Nain Xu, Zhong-Quan Gu, Xue-Fu Zhong, and WY Ching. Ab initio calculations for the neutral and charged O vacancy in sapphire. *Physical Review B*, 56(12):7277, 1997.
- [64] Yinkai Lei, Yu Gong, Zhiyao Duan, and Guofeng Wang. Density functional calculation of activation energies for lattice and grain boundary diffusion in alumina. *Physical Review B*, 87(21):214105, 2013.
- [65] JR Gladden, Jin H So, JD Maynard, PW Saxe, and Y Le Page. Reconciliation of ab initio theory and experimental elastic properties of Al_2O_3 . *Applied Physics Letters*, 85(3):392–394, 2004.
- [66] Takayasu Goto, Orson L Anderson, Ichiro Ohno, and Shigeru Yamamoto. Elastic constants of corundum up to 1825 K. *Journal of Geophysical Research: Solid Earth*, 94(B6):7588–7602, 1989.
- [67] Ioannis Manassidis and Michael J Gillan. Structure and energetics of alumina surfaces calculated from first principles. *Journal of the American Ceramic Society*, 77(2):335–338, 1994.
- [68] Arnaud Marmier and Stephen C Parker. Ab initio morphology and surface thermodynamics of $\alpha - \text{Al}_2\text{O}_3$. *Physical Review B*, 69(11):115409, 2004.
- [69] Jizhong Sun, T Stirner, and A Matthews. Structure and surface energy of low-index surfaces of stoichiometric $\alpha - \text{Al}_2\text{O}_3$ and $\alpha - \text{Cr}_2\text{O}_3$. *Surface and Coatings Technology*, 201(7):4205–4208, 2006.
- [70] Henry P Pinto, Risto M Nieminen, and Simon D Elliott. Ab initio study of $\gamma - \text{Al}_2\text{O}_3$ surfaces. *Physical Review B*, 70(12):125402, 2004.
- [71] Takahiro Kurita, Kazuyuki Uchida, and Atsushi Oshiyama. Atomic and electronic structures of $\alpha - \text{Al}_2\text{O}_3$ surfaces. *Physical Review B*, 82(15):155319, 2010.
- [72] Guoyin Shen and Peter Lazor. Measurement of melting temperatures of some minerals under lower mantle pressures. *Journal of Geophysical Research: Solid Earth*, 100(B9):17699–17713, 1995.
- [73] Guoyin Shen and Peter Lazor. Measurement of melting temperatures of some minerals under lower mantle pressures. *Journal of Geophysical Research: Solid Earth*, 100(B9):17699–17713, 1995.
- [74] H Sakate, F Sakuma, and A Ono. Observation of Al_2O_3 melting and freezing plateaus using a cavity-type tungsten crucible. *Metrologia*, 32(2):129, 1995.

- [75] Rajeev Ahuja, AB Belonoshko, and Börje Johansson. Melting and liquid structure of aluminum oxide using a molecular-dynamics simulation. *Physical Review E*, 57(2):1673, 1998.
- [76] BWH Van Beest, Gert Jan Kramer, and RA Van Santen. Force fields for silicas and aluminophosphates based on ab initio calculations. *Physical Review Letters*, 64(16):1955, 1990.
- [77] Shuji Ogata, Hiroshi Iyetomi, Kenji Tsuruta, Fuyuki Shimojo, Aiichiro Nakano, Rajiv K Kalia, and Priya Vashishta. Role of atomic charge transfer on sintering of TiO₂ nanoparticles: variable-charge molecular dynamics. *Journal of Applied Physics*, 88(10):6011–6015, 2000.
- [78] Jülich Supercomputing Centre. JURECA: Modular supercomputer at Jülich Supercomputing Centre. *Journal of Large-scale Research Facilities*, 4(A132), 2018. doi: 10.17815/jlsrf-4-121-1. URL <http://dx.doi.org/10.17815/jlsrf-4-121-1>.
- [79] M Bauchy. Structural, vibrational, and elastic properties of a calcium aluminosilicate glass from molecular dynamics simulations: the role of the potential. *The Journal of Chemical Physics*, 141(2):024507, 2014.

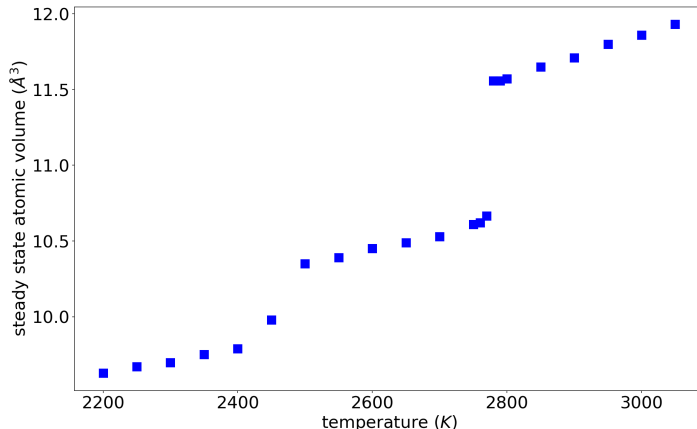
Appendix

Vashishta [24]	Al	O	Al-Al	Al-O	O-O	Al-O-Al	O-Al-O
Z (e)	1.5237	-1.0158					
η_{ij}			7	9	7		
H_{ij} (eV \AA)			12.7506	249.3108			
D_{ij} (eV \AA^4)			0	50.1522	44.5797		
W_{ij} (eV \AA^6)			0	0	79.2884		
B_{ijk} (eV)						8.1149	12.4844
$\bar{\theta}_{ijk}$ (deg)						109.47	90.0
C_{ijk}						10	10
γ (\AA)						1	1
r_0 (\AA)						2.9	2.9
Coul-Buck [28]							
Z (e)	1.4175	-0.945					
A (eV)			31574470	28480	6463.4		
ρ (\AA)			0.068	0.172	0.276		
C (eV \AA^6)			14.07	34.63	85.22		
B-M-H [79]							
Z (e)	1.8	-1.2					
A (eV)			0.002896	0.007489	0.011984		
ρ (\AA)			0.0680	0.1640	0.2630		
σ (\AA)			1.5704	2.6067	3.6430		
C (eV \AA^6)			14.0305	34.5272	84.9671		
D (eV \AA^8)			0	0	0		
CTI+EAM [26, 35]							
χ (eV)	0	5.484763					
J (eV)	10.328655	14.035715					
γ (\AA^{-1})	0	0					
ζ (\AA^{-1})	0.968438	2.143957					
Z (e)	0.763905	0					
r_e (\AA)				2.511075	3.315171		
α				8.574224	5.716137		
β				4.669743	3.758299		
A (eV)				0.208662	0.263795		
B (eV)				0.678293	0.273569		
κ				0.355898	0.498438		
λ				1.014487	0.560282		

Table 2: The potential parameters of four potentials. The parameters for CTIE are from the original source [26] and the parameters of EAM potential are from Ref. [35].

Supplementary Material

0.0.1. Method of calculating melting temperature An energetically minimized periodic alumina system is heated up to several temperatures for allowing volume expansion and equilibrated by NPT at the target temperatures for minimum of 100 ps. The steady state volume per atom is plotted against temperatures for VASH in Fig. S1 as an example.



Supplementary Figure S1: The steady state volume per atom, obtained at various temperatures for VASH potential, is plotted with temperature. The window of temperature within which the volume jump occurs is considered to be the melting temperature of the potential. The melting temperature is 2760 K for VASH potential associated with the biggest jump in volume per atom as shown in the figure.

1. Information concerning the computation of material properties at 0 K

1.1. Lattice constants, cohesive energy and vacancy formation energy

A 3D alumina system of 8640 atoms (3456 Al + 5184 O) atoms, periodic in all directions are energetically minimized to calculate the energy per atom (cohesive energy) and lattice constants. The vacancy formation energy is calculated by taking a difference in energy between a minimized infinite pristine system and with a vacancy in it.

1.2. Surface energies

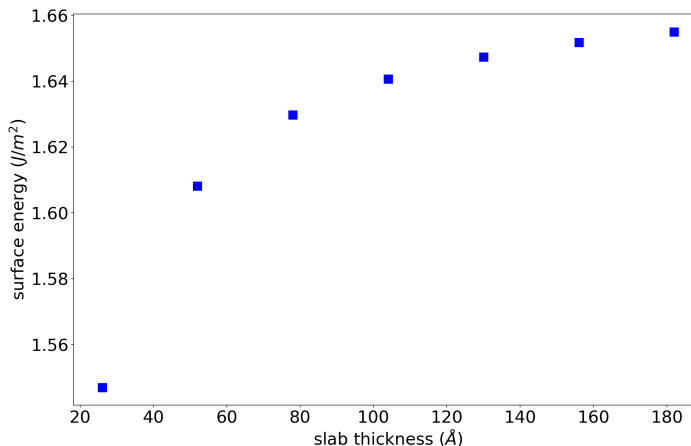
For surface energy calculations, infinite slabs with the desired crystallographic orientations in the free surface direction are minimised in energy. The value of the surface energy is then

calculated as:

$$\gamma = \frac{E_{\text{slab}} - E_{\text{coh}}N}{2A}, \quad (1)$$

where E_{slab} is the energy of the slab, E_{coh} is the cohesive energy, A is the free surface area, and N is the total number of atoms in the slab.

1.2.1. Identifying the appropriate slab thickness In order to minimise the influence of the thickness on the calculated surface energy, the same calculation is performed for several slab thicknesses. The calculated surface energy increases with the slab thickness, and it stabilises with respect to thickness beyond a certain value (see Fig. S2). Based on this study, around 60 Å is chosen for the minimum slab thickness to calculate surface energies.



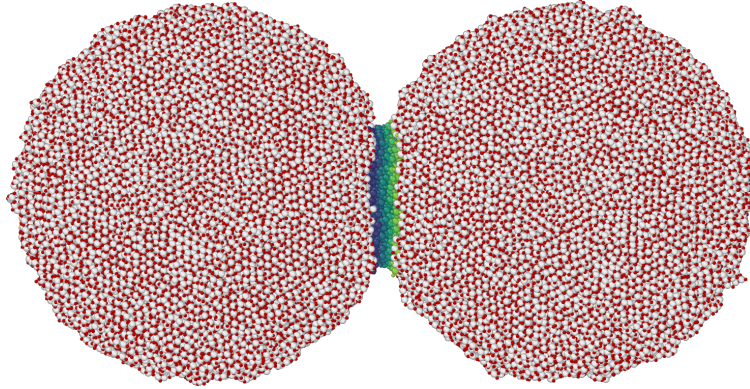
Supplementary Figure S2: Surface energy of [0001] for slabs of different thicknesses calculated with VASH potential.

1.3. Elastic constants

The system is deformed by applying a small strain in positive and negative Voigt strain directions. The elastic constants are calculated by taking the derivatives of the measured change in stress tensor with respect to strain.

1.4. Neck region

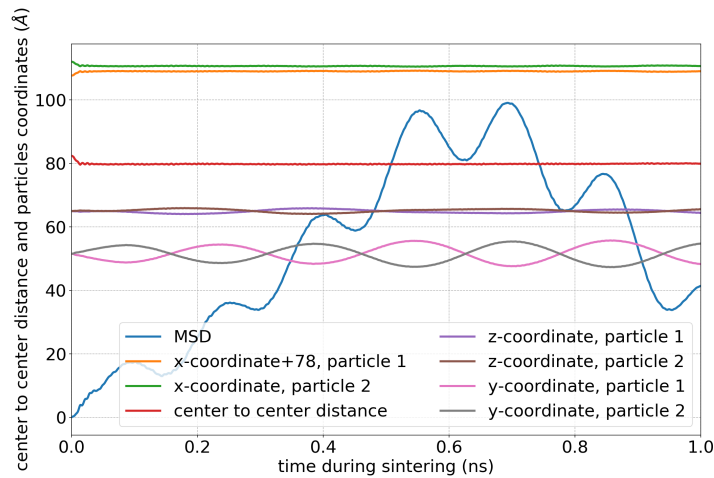
In Fig. S3 the neck region of the sintering nanoparticles is highlighted by blue to green contour for $R = 6$ nm particle and VASH. The details on defining a neck region is described in the main text.



Supplementary Figure S3: The neck region between two particles during sintering (highlighted with a color gradient). All other atoms are colored according to their chemical species: Al - gray, O - red.

1.5. Influence of rigid body motion of particles on MSD

Fig. S4 shows the centre-to-centre distance and particle coordinates as a function of the sintering time.



Supplementary Figure S4: The rigid body motion of particles contribute to the MSD calculation. The centre-to-centre distance between particles remains almost unchanged. The centre of masses of the particles do not change substantially in x and z direction. The particles oscillate with respect to their centre point in the y direction resulting a local fluctuation in MSD.